Dalton Transactions

ROYAL SOCIETY OF CHEMISTRY

PAPER

View Article Online
View Journal | View Issue

Cite this: *Dalton Trans.*, 2020, **49**, 5597

A synthetic manganese–calcium cluster similar to the catalyst of Photosystem II: challenges for biomimetic water oxidation†

Younes Mousazade,[a] Mohammad Reza Mohammadi,[b] Robabeh Bagheri,[c] Rahman Bikas, *[d] Petko Chernev, [e,f] Zhenlun Song, [c] Tadeusz Lis,[g] Milosz Siczek, [g] Nader Noshiranzadeh, [h] Stefan Mebs,[e] Holger Dau, [e] Ivelina Zaharieva [e] and Mohammad Mahdi Najafpour *[a,i,j]

Received 13th February 2020,
Accepted 19th March 2020

DOI: 10.1039/d0dt00536c

rsc.li/dalton

Herein, we report the synthesis, characterization, crystal structure, density functional theory calculations, and water-oxidizing activity of a pivalate Mn–Ca cluster. All of the manganese atoms in the cluster are Mn(IV) ions and have a distorted MnO_6 octahedral geometry. Three Mn(IV) ions together with a Ca(II) ion and four-oxido groups form a cubic Mn_3CaO_4 unit which is similar to the Mn_3CaO_4 cluster in the water-oxidizing complex of Photosystem II. Using scanning electron microscopy, transmission electron microscopy, energy dispersive spectrometry, extended X-ray absorption spectroscopy, chronoamperometry, and electrochemical methods, a conversion into nano-sized Mn-oxide is observed for the cluster in the water-oxidation reaction.

Introduction

A manganese–calcium cluster is the active site of water oxidation in Nature and thus, manganese–calcium compounds are of special interest as water-oxidation catalysts in conjunction with the conversion of solar energy into chemical energy in artificial photosynthetic systems. Water splitting towards hydrogen production is a promising technique to generate energy from renewable sources.[1–4] Although in water splitting the cathodic reaction is of major interest in hydrogen production, anodic water oxidation, being a complicated four proton–four electron reaction, is important for ensuring the efficiency of hydrogen generation as it typically requires the application of large overpotentials.[5,6] It is also a process of relevance to N_2 fixation and CO_2 reduction as water is the ultimate source of reducing equivalents (electrons and protons) for these processes.

In plants, algae, and cyanobacteria, Nature uses a unique water-oxidizing complex (WOC) for water oxidation.[7–9] It is a μ-oxido (μ-O^{2-}) bridged $CaMn_4O_5$ cluster, coordinated by carboxylate and imidazole from the surrounding amino acids.[7–11] So, the use of metal-oxo clusters could be an interesting strategy to mimic the WOC. Only a few stable structural models for this cluster have been reported.[12–18] The closest structural mimic so far was reported by Zhang *et al.*, but it is unstable in aqueous solutions.[18]

There are many molecular systems to catalyze water oxidation,[19–24] and Mn complexes[24–33] are among the most

[a]*Department of Chemistry, Institute for Advanced Studies in Basic Sciences (IASBS), Zanjan, 45137-66731, Iran. E-mail: mmnajafpour@iasbs.ac.ir; Tel: +98 24 3315 3201*
[b]*University of Sistan and Baluchestan, Department of Physics, 98167-45845 Zahedan, Iran*
[c]*Surface Protection Research Group, Surface Department, Ningbo Institute of Materials Technology and Engineering, Chinese Academy of Sciences, 519 Zhuangshi Road, Ningbo 315201, China*
[d]*Department of Chemistry, Faculty of Science, Imam Khomeini International University, 34148-96818 Qazvin, Iran. E-mail: bikas@sci.ikiu.ac.ir; Tel: +98 28 3390 1368*
[e]*Freie Universität Berlin, Fachbereich Physik, Arnimallee 14, 14195 Berlin, Germany*
[f]*Uppsala University, Department of Chemistry – Ångströmlaboratoriet, Lägerhyddsvägen 1, 75120 Uppsala, Sweden*
[g]*Faculty of Chemistry, University of Wrocław, 14. Joliot-Curie, 50-383 Wrocław, Poland*
[h]*Department of Chemistry, Faculty of Science, University of Zanjan, 45371-38791 Zanjan, Iran*
[i]*Center of Climate Change and Global Warming, Institute for Advanced Studies in Basic Sciences (IASBS), Zanjan, 45137-66731, Iran*
[j]*Research Center for Basic Sciences & Modern Technologies (RBST), Institute for Advanced Studies in Basic Sciences (IASBS), Zanjan 45137-66731, Iran*

†Electronic supplementary information (ESI) available: Details of experiments, selected bond lengths and bond angles, parameters obtained by the simulation of the k^3-weighted EXAFS spectra, electronic distribution of frontier orbitals of **1**, frontier orbital energies of **1**, XPS, and SEM-EDX images. CCDC 1920522. For ESI and crystallographic data in CIF or other electronic format see DOI: 10.1039/D0DT00536C

investigated molecular catalysts for water oxidation. However, finding kinetically dominant catalysts for the water-oxidation reaction is a challenge. In the search for a functional mimic of the natural paragon, a series of $Mn_{12}O_{12}(OC)_{16-x}L_x(H_2O)_4$ complexes (L = acetate, benzoate, benzenesulfonate, diphenylphosphonate, dichloroacetate) deposited on a fluorine-doped tin oxide (FTO) glass electrode were investigated as water-oxidizing catalysts.[34] At least a single one-electron oxidation is needed to activate these catalysts toward water oxidation.[34] Why "at least one-electron oxidation" is needed, can be an enigma. In general, the reported Mn oxido clusters typically show no water-oxidation activity or indicate water-oxidation at a high overpotential. Among the synthetic molecular catalysts active in water oxidation, an $[Mn_{12}O_{12}(O_2CC_6H_3(OH)_2)_{16}(H_2O)_4]$ complex with high solubility in water is proposed for water oxidation with a very low overpotential for the onset of water oxidation (334 mV at pH 6).[35] Recently, it has been reported that a homogeneous Mn cluster shows water oxidation at pH 6 with a turnover frequency of 22 s^{-1}, a high faradaic efficiency of 93% and an overpotential of only 74 mV for the onset of water oxidation.[13]

An additional complication hampering the development of efficient Mn-based molecular catalysts for water oxidation is the instability of the complexes in the presence of chemical oxidants.[36–38] In many cases, the starting molecular complex is decomposed into a nano-sized metal oxide as the true catalyst for water oxidation.[37] Regardless of this stability problem, finding a true molecular catalyst can be important for designing efficient and stable catalysts for water oxidation.[39]

Herein, an Mn–Ca cluster $[Mn_6Ca_4(\mu\text{-}O)_8(OAc)_2(Piv)_{14}(HPiv)_4(H_2O)_{0.3}]\cdot CH_3CN$ (HPiv: pivalic acid) (**1**) was synthesized, characterized and investigated under electrochemical water-oxidation conditions. It is interesting that our new synthesized cluster is a dimer of a previously reported $[Mn^{IV}_3Ca_2O_4(O_2CBu^t)_8(Bu^tCO_2H)_4]$ cluster,[17] which shows that such structures may be aggregated to form multimeric structures.

Results and discussion

Synthesis and crystal structure

The reaction of $KMnO_4$, $Mn(OAc)_2\cdot 4H_2O$, $Ca(OAc)_2\cdot H_2O$ and pivalic acid in acetonitrile gave red crystals of **1**. The complex was characterized by elemental analysis, spectroscopic

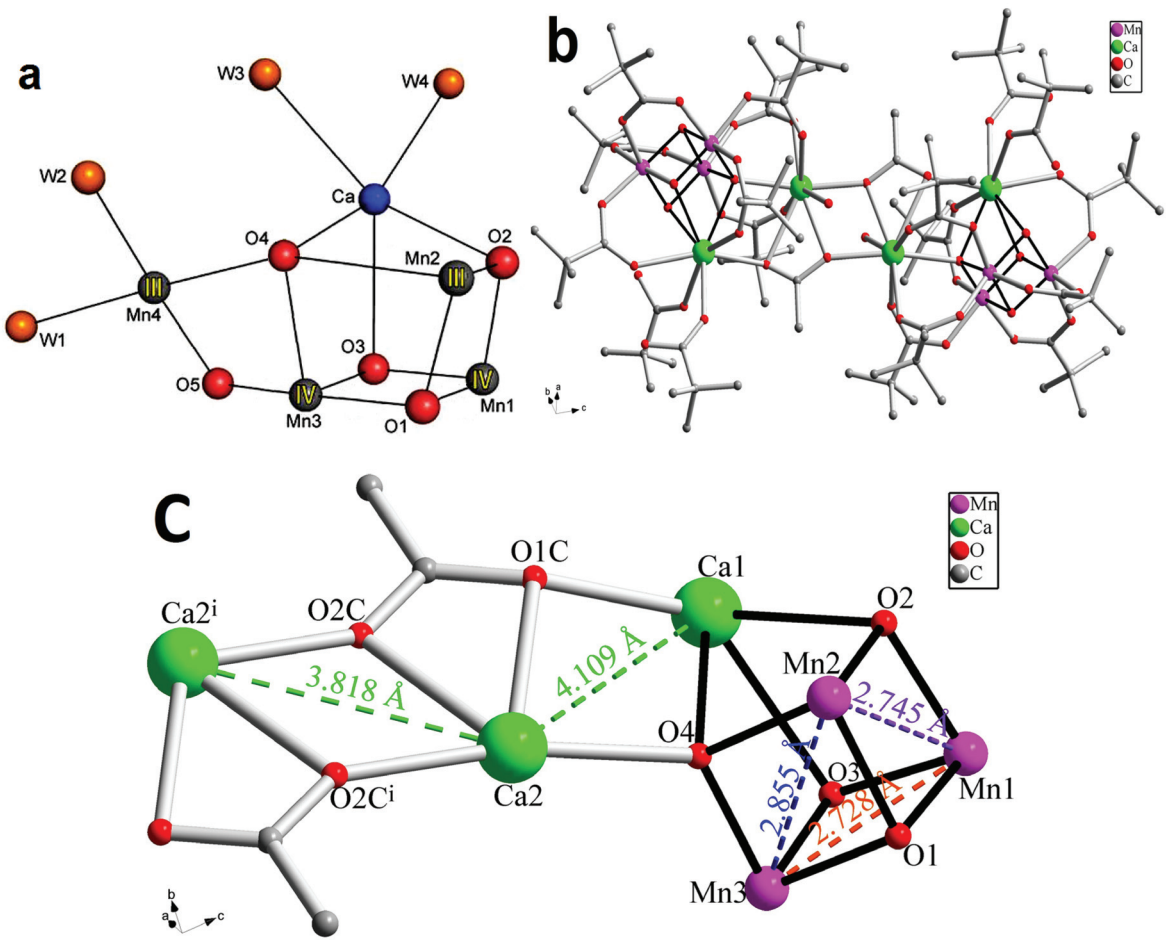

Fig. 1 The WOC in PSII (from ref. 9) (a). Structure of **1** (b and c). The cubic unit for **1** is shown by black lines (b and c); the hydrogen atoms, disordered parts and solvent molecules are removed for clarity. Image (a) is from ref. 9. Copyright (2015) by Springer Nature Publishing Group.

methods, and single-crystal X-ray diffraction. In the FT-IR spectrum of **1**, the strong bands at 1639–1714 cm^{-1} are due to the vibration of the C–O groups of coordinated carboxylate groups. The broadband at 3447 cm^{-1} can be attributed to the O–H group of coordinated pivalic acid ligands, which is involved in hydrogen bonding interactions (see the Experimental section for FTIR details). The structure of **1** with the atom-numbering scheme is shown in Fig. 1 and the selected bond lengths and angles around the manganese ions are summarized in Tables 1 and S1† Single-crystal X-ray analysis indicated that **1** is a neutral centrosymmetric Mn_6Ca_4 cluster wherein the metal atoms are coordinated by the oxido ligands and carboxylate groups of pivalate and acetate anions. The asymmetric part of **1** contains an Mn_3Ca_2 cluster (see Fig. 1b). The acetate anions coordinated to Ca2 act as a bridging group between the two parts of the cluster. All of the manganese ions in **1** are Mn(IV) ions and have a distorted octahedral geometry with an MnO_6 coordination environment. The bond lengths around the Mn

Table 1 Comparison between the bond lengths and metal–metal distances in the crystal structure of compound **1** and the WOC in PS II[9]

Bond	1	WOC PSII	1 (DFT)	Bond	1	WOC PSII	1 (DFT)
Mn1–Mn2	2.745(1)	2.68(5)	2.739	Mn2–O1	1.879(2)	1.82(7)	1.865
Mn1–Mn3	2.728(1)	2.70(3)	2.719	Mn2–O2	1.859(2)	1.83(7)	1.856
Mn2–Mn3	2.855(1)	3.20(8)	2.857	Mn2–O4	1.856(2)	2.02(6)	1.850
Mn1–Ca1	3.399(1)	3.47(3)	3.443	Mn3–O1	1.895(2)	1.90(2)	1.894
Mn2–Ca1	3.389(2)	3.40(6)	3.527	Mn3–O3	1.838(3)	1.90(12)	1.823
Mn3–Ca1	3.377(2)	3.32(3)	3.428	Mn3–O4	1.863(2)	2.20(14)	1.871
Mn1–O1	1.890(2)	1.80(5)	1.881	Ca1–O2	2.444(2)	2.54(8)	2.547
Mn1–O2	1.844(2)	2.70(1)	1.841	Ca1–O3	2.483(3)	2.61(3)	2.518
Mn1–O3	1.813(2)	1.87(8)	1.796	Ca1–O4	2.574(3)	2.67(6)	2.696

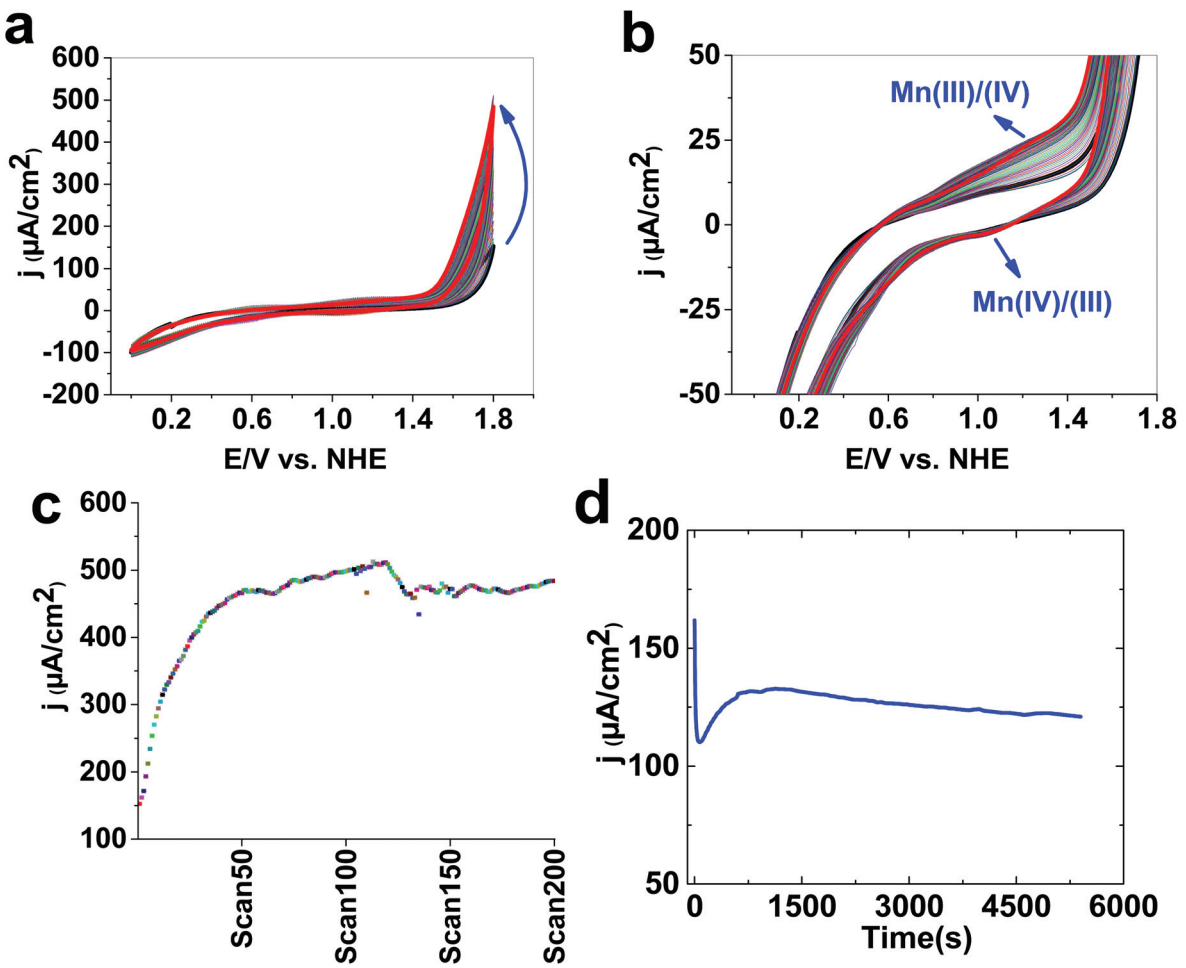

Fig. 2 Continuous CVs of **1** on FTO in 25.0 mL of phosphate buffer (1.0 M, pH = 11.0) (a and b). The current *vs.* scan plot for the continuous CVs at 1.8 V (c). Amperometry was performed in the presence of **1** at 1.8 V in 25.0 mL of phosphate buffer (1.0 M, pH = 11.0) (d).

ions are in the range of 1.81–1.98 Å, which is the normal range reported for Mn(IV) complexes.[19–24] Three Mn(IV) ions together with a Ca(II) ion and four oxido groups form a cubic Mn_3CaO_4 unit, which is similar to the Mn_3CaO_4 unit observed in the water-oxidizing complex (WOC) of Photosystem II (PSII) (see Fig. 1). Similar to the WOC of PS II, the Mn(IV) ions are connected together by oxido and carboxylate groups with the Mn1···Mn2, Mn1···Mn3 and Mn2···Mn3 distances of 2.745(1), 2.728(1) and 2.855(1) Å, respectively. Table 1 shows the comparison of the geometrical parameters around the metal ions in **1** with those in the Mn_3CaO_4 unit of the WOC of PS II which indicates that the atomic distances in **1** are very close to the geometrical parameters of the Mn_3CaO_4 unit of the WOC in PS II.

In **1** the Ca(II) ions have a CaO_8 coordination environment. Two Ca ions (Ca1 and Ca2) are connected together by the oxido ligands and oxygen atoms of bridging acetate groups. The same acetate ligand also acts as a bridging group between two Ca2 ions and consequently, it is a bridging group between three Ca ions. The Ca1···Ca2 and Ca2···Ca2^{i} distances are 4.109(2) and 3.818(2) Å, respectively. There is an acetonitrile solvent molecule in the crystal packing of **1**, which is stabilized by hydrogen bonding interactions. The Ca2 atom and the $-CH_3$ groups of one of the pivalic acid molecules connected to Ca1 are disordered. In the structure of **1** the disordered parts and also the hydrogen atoms are eliminated for clarity as shown in Fig. 1.

To model the atomic coordinates, density functional theory (DFT) calculations were conducted for the gas-phase molecular

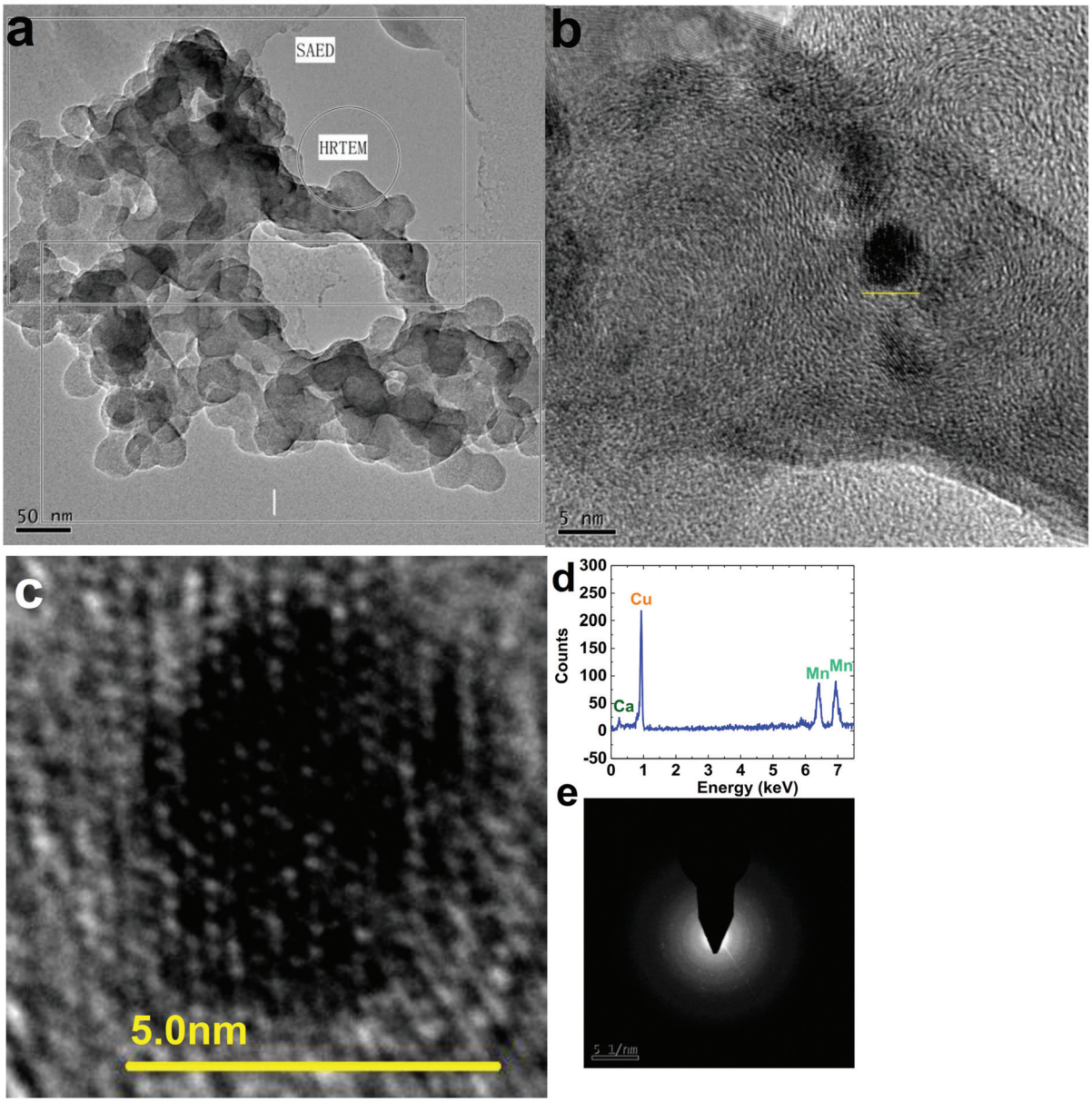

Fig. 3 (HR)TEM images of **1** before the water-oxidation reaction (a–c). TEM-EDX (d) and SAED (e) for **1** before the water oxidation reaction.

structure of **1** at the b3pw91/6-31+G* level of theory using Gaussian16.[40] Anti-ferromagnetic coupling was taken into account by the broken-symmetry approach and appropriate assignment of molecular fragments. Due to the large size of the model (330 atoms), normal mode analysis was not feasible. Relevant atom–atom distances are listed in Table 1. Occupied frontier orbitals are dominated by contributions from the oxygen atoms of the Mn_3Ca clusters and adjacent carboxylate groups, whereas unoccupied frontier orbitals are dominated by contributions from the Mn and O atoms (see Fig. S1 and S2†).

Water oxidation studies

To study the behaviour of **1** as a possible catalyst for electrochemical water oxidation, small crystals of **1** were placed (see the ESI†) on the surface of an FTO-coated glass electrode. By scanning electron microscopy (SEM), transmission electron microscopy (TEM), energy dispersive spectrometry (EDX), X-ray absorption near edge structure (XANES), extended X-ray absorption fine structure (EXAFS), chronoamperometry, and other electrochemical methods, it is indicated that for such a cluster, not the molecular compound but the nano-sized Mn

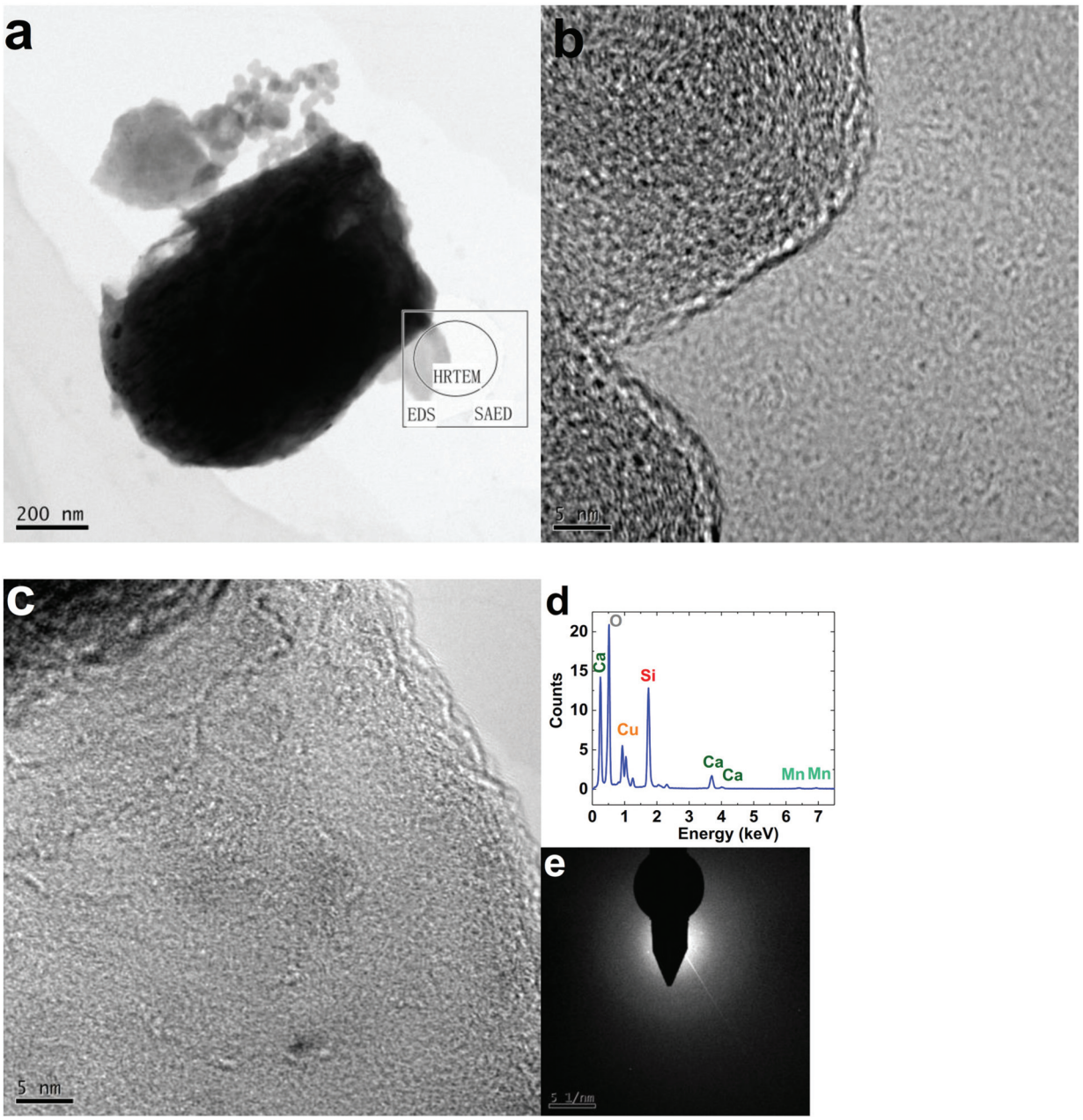

Fig. 4 (HR)TEM images of **1** after the water-oxidation reaction (a–c). TEM-EDX (d) and SAED (e) for **1** after the water-oxidation reaction. Amperometry was performed in the presence of **1** at 1.8 V in 25.0 mL of phosphate buffer (1.0 M, pH = 11.0).

oxide formed at high pH upon the application of oxidizing potentials is the true catalyst for water oxidation.

At pH = 7, no water oxidation was observed even at a high overpotential (>1 V; all data reported *vs.* NHE). At pH = 11 and a low overpotential, no water oxidation was observed. However, at pH = 11 and a high overpotential (>1 V), a catalytic wave was observed in the CV with continuously increasing amplitudes during the first 50 cycles (Fig. 2a and b). These electrochemical experiments show, as previously reported,[41] that the Mn clusters need "an activation" potential to initiate water oxidation. Such activation could be achieved by a sequence of CVs. We have tried to find why an activation potential is needed for this Mn cluster. The continuous CV of **1** showed the growth of the peaks related to Mn(II)/(III) and Mn(III)/(IV) at 0.63 and 1.19 V, respectively (all data in the paper were reported *vs.* NHE). We attribute these peaks to Mn oxidation in Mn oxides (Fig. 2b).[41]

Chronoamperometry (1.8 V for 1.5 hours in 1.0 M phosphate buffer, pH 11) shows an immediate increase after applying the potential (Fig. 2d). This increase is probably because of the formation of a more active catalyst for the water-oxidation reaction. After 700 s the conversion is almost completed and after this time the newly formed compound would be responsible for electrocatalytic water oxidation.

XPS for **1** performed before CV showed O, C, Mn and Ca on the surface (Fig. S3†). The Mn 2p area consists of a spin–orbit doublet attributed to the Mn $2p_{3/2}$ and Mn $2p_{1/2}$ states at around 642 and 652 eV, respectively, which are mainly composed of Mn (IV)[42] (Fig. S3†). As reported previously, the Ca 2p region was observed at 347 eV and has well separated spin–orbit components (Δ = 3.5 eV). The O 1s spectrum can be deconvoluted into several peaks, and each peak corresponds to the binding energies of μ-O, OH^- and H_2O. The C–C bond and carboxylate groups were observed in the C 1s area. In the XPS spectra of complex **1** obtained after the electrochemical water-oxidation reaction (after chronoamperometry at 1.8 V for 1.5 hours in 1 M phosphate buffer, pH 11), there are no significant changes, however, K 2p displayed the presence of potassium on the surface of the compound after the reaction (see Fig. S4†). Other techniques, however, indicate that there are more significant changes in the material.

The SEM-EDX data for **1** obtained after chronoamperometry indicated that the compound contains C (~33.43%), O (46.96%), Mn (~15.26%) and Ca (~4.36%). Thus, the formula of the surface of FTO in the presence of **1** can be written as $Mn_{3.5}CaC_{7.7}O_{10.77}$. These changes are accompanied by the changes in morphology. After the water-oxidation reaction, the nanoparticles (*ca.* 20–30 nm) with no well-defined morphology were observed on the surface of FTO. These nanoparticles were aggregated to form a complicated structure (Fig. 3 and S5†). Before the water-oxidation reaction, in a few areas, HRTEM indicated the lattice fringes with interplanar distances of 3.0–3.4 Å related to **1**, which is consistent with the powder XRD data (2Θ = 26–29°). The selected area electron diffraction (SAED) pattern shown in Fig. 3 consists of diffuse rings that indicate a pattern typical of **1**.

The (HR)TEM images of the mechanically separated solid from the operated FTO after water oxidation at 1.8 V for 1.5 hours displayed a highly amorphous material (Fig. 4). SAED also showed a pattern typical of an amorphous material.

In the next step, X-ray absorption spectroscopy (XAS) was performed to determine the structural changes after the water-oxidation reaction at the atomic level. The XANES experiment

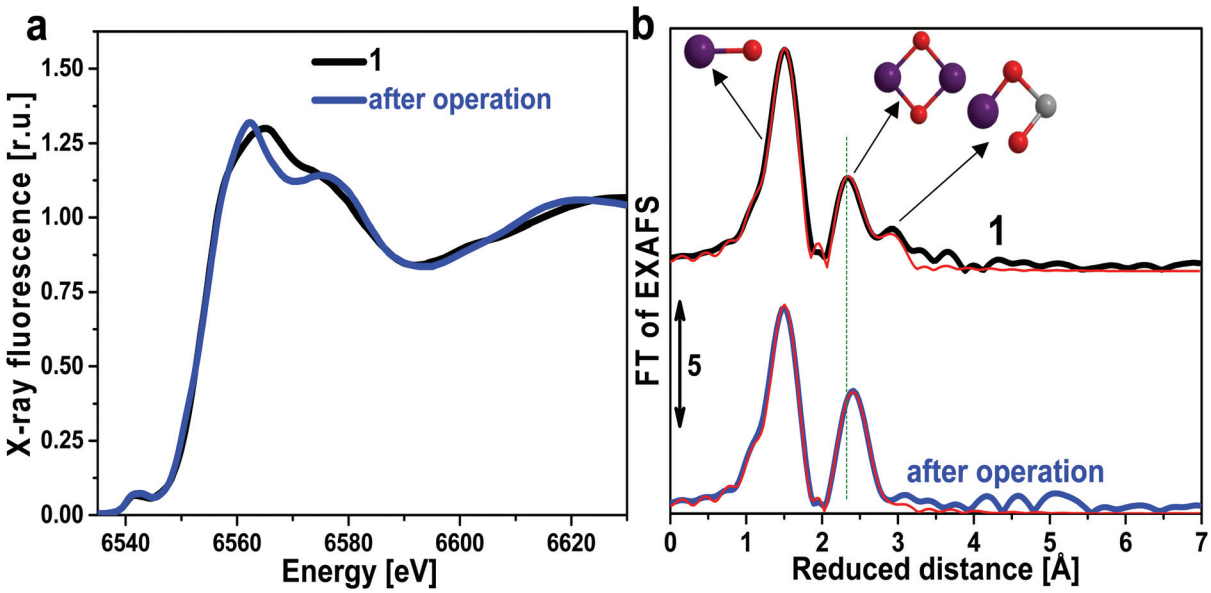

Fig. 5 XANES spectra (a) and Fourier-transform of EXAFS (b) spectra of the synthesized complex **1** (black) and the operated sample under amperometry conditions (blue; amperometry was performed in the presence of **1** at 1.8 V in 25.0 mL of phosphate buffer (1.0 M, pH = 11.0), respectively. The thick lines show experimental data, and the thin red lines show simulations. The phase shift was not corrected. The k^3-weighted EXAFS oscillations are shown in Fig. S7.† The fit parameters for the simulations are given in Table S2.† The identified structural motifs are displayed schematically. Color codes are the following: manganese, purple, oxygen, red and carbon, grey. In summary, X-ray absorption spectroscopy shows that after the operation, **1** converts to MnO_x which is likely the dominant water-oxidizing catalyst.

showed that the average oxidation states of **1** and the operated sample are the same ($Mn^{3.9+}$; Fig. 5a and S6†). However, after the operation, the shape of the edge changed, suggesting the structural changes in the material.

The Fourier transform of the EXAFS-spectra of **1** before and after the operation showed a high main Mn–O peak that in both cases corresponds to octahedrally coordinated Mn ions. This peak can be simulated by one Mn–O shell at 1.89 Å for **1** and for the operated sample (after amperometry at 1.8 V for 1.5 hours). The second peak in the Fourier transform (appearing at a reduced distance of 2.3 Å in Fig. 5b) originates mainly from Mn–Mn coordination at a 2.77 Å average distance for **1** and at 2.81 Å for the operated sample (Table S2†) and likely corresponds to di-μ-oxo bridged Mn ions. A smaller third peak at a reduced distance of 2.9 Å is visible only for **1** and can be simulated by Mn–C and Mn–O shells at 2.91 and 3.16 Å, corresponding to the C and O atoms of the pivalic acid ligands and to O along the main diagonal of the cubic unit. These shells are missing from the operated sample, and therefore we conclude that the pivalic acid ligands are no longer connected to the Mn centers.

Compound **1** is an interesting model for the WOC in PSII. Unlike other close structural mimics of the Mn_4CaO_5 cluster in PSII (*e.g.* complex from Zhang's group[18]), this complex is stable in aqueous solutions – a basic requirement to be used as a water-oxidizing catalyst. However, a high overpotential is a problem for this cluster as at a high overpotential, the cluster is decomposed. It is clear that the polypeptide around the Mn cluster is important for both the stabilization of the Mn_4CaO_5 cluster in the biological system and the decrease in the overpotential for water oxidation.[7–9,43] Also, it seems that the decomposition reaction is an important issue in the WOC of PSII, but Nature uses a complicated self-healing mechanism to repair the biological water-oxidizing cluster.[44]

Conclusions

In conclusion, we reported an artificial model for the WOC in PSII. We suggest that the carboxylate groups bound to a large hydrophobic complex could host Mn_3Ca units as observed in PSII. However, under water-oxidation conditions, the cluster is decomposed to Mn oxide and the latter is likely responsible for the observed water-oxidation activity. Compared to the WOC in PSII, such artificial models would need to have a very stable ligand or the cluster should oxidize water at a lower overpotential to prevent ligand oxidation. Alternatively, a self-healing mechanism would be needed for sustained activity. Channels to remove H^+ and O_2 and for access to water molecules, as they exist in PSII, may be necessary for these artificial models.

Experimental

Materials and instrumentation

$KMnO_4$ (Merck; Reag. Ph. Eur.), $Mn(OAc)_2{\cdot}4H_2O$ (Sigma-Aldrich; ≥99%), $Ca(OAc)_2{\cdot}H_2O$ (Sigma-Aldrich; ACS reagent, ≥99.0%) and pivalic acid (Merck; synthesis grade) were purchased from Sigma-Aldrich or Merck companies. TEM was carried out with an FEI Tecnai G^2 F20 transmission electron microscope (TF20 200 kV). SEM and EDX were carried out with a VEGA\TESCAN-XMU. X-ray powder patterns were recorded with a Bruker, D8 ADVANCE (Germany) diffractometer (CuK_α radiation). Electrochemical experiments were performed using an $EmStat^{3+}$ from the PalmSens Company (the Netherlands). Fluorine-doped tin oxide (FTO) and Pt foil were used as a working and an auxiliary electrode, respectively. Elemental analysis (carbon, hydrogen, and nitrogen) was performed using a Carlo ERBA Model EA 1108 analyzer.

Synthesis of $[Mn_6Ca_4(\mu\text{-}O)_8(OAc)_2(Piv)_{14}(HPiv)_4(H_2O)_{0.3}]{\cdot}CH_3CN$ (1)

1 was synthesized from the reaction of $KMnO_4$ (4 mmol), $Mn(OAc)_2{\cdot}4H_2O$ (2 mmol), $Ca(OAc)_2{\cdot}H_2O$ (2 mmol) and pivalic acid (20 mmol) in acetonitrile by using a branched tube. Mentioned amounts of materials were added to the main arm of the branched tube and the tube was carefully filled with acetonitrile. The tube was sealed and the reagent containing arm immersed in an oil bath at 60 °C. Firstly, the solution was colorless, but after 5 hours its color changed to dark-purple and then to dark red. Some amounts of cubic-shaped red crystals were formed in the cooler arm after about 12 hours and their amount increased after three days. The crystals were filtered off, washed with a little amount of cooled acetonitrile and dried at room temperature. Yield: 80%. Anal. calc. for $C_{96}H_{175.60}Ca_4Mn_6NO_{48.30}$ (M_W = 2606.72): C, 44.23; H, 6.79; N, 0.54; Ca, 6.15; Mn, 12.65. Found: C, 44.37; H, 6.84; N, 0.39; Ca, 6.09; Mn, 12.72%. FT-IR (Nujol, cm^{-1}): 3447 (m, br), 2958 (vs), 2855 (vs), 1714 (s), 1690 (s), 1639 (vs), 1559 (vs), 1510 (m), 1483 (vs), 1459 (s), 1411 (vs), 1374 (s), 1346 (s), 1222 (vs), 1030 (w), 938 (w), 896 (w), 869 (w), 786 (w), 758 (w), 619 (vs), 594 (s), 534 (m), 447 (m).

Cyclic voltammetry and amperometry

For the investigation of the electrochemical behavior of **1**, cyclic voltammetry (CV) in a three-electrode cell was performed in which Ag/AgCl, a platinum sheet, and FTO were used as the reference, the counter, and the working electrode, respectively. 3.0 mg (1.25 μmol) of **1** was added to 30 mL of water and dispersed by sonication and then this dispersed mixture (30 μL) was dropped on an FTO electrode (1.0 cm^2) and dried at ambient temperature. Then, 10 μL of Nafion solution (10% in methanol) was dropped on the catalyst surface and dried at room temperature. Cyclic voltammetry was performed in the range of 0.0 to 1.6 V (*vs.* Ag/AgCl) at room temperature and at a 50 mV s^{-1} scan rate in phosphate buffer (1.0 M, pH = 11). 50 cycles of measurement were continued to follow the cluster behavior in a long-term operation. The same measurement was performed for FTO without **1**. After the electrochemical measurement, all potentials were converted to the NHE reference electrode scale.

XAS measurements

3.0 mg (1.25 μmol) of **1** was added to 30 mL of water and dispersed by sonication and then this dispersed mixture (30 μL)

was dropped on an FTO electrode (1.0 cm^2) and dried at ambient temperature. Then, 10 μL of Nafion solution (10% in methanol) was dropped on the catalyst surface and dried at room temperature. The amperometry measurement at 1.8 V for two hours was performed in a solution of phosphate buffer (1.0 M, pH 11) and by using Ag/AgCl and a platinum sheet as the reference and auxiliary electrodes, respectively. XAS measurements (EXAFS and XANES) at the manganese K-edges for the obtained sample after amperometry and for the sample before amperometry were performed at the KMC-3 beamline at the BESSY II synchrotron facility (Helmholtz-Zentrum Berlin, Germany) at 20 K using a liquid-helium cooled cryostat (Oxford-Danfysik).

The angle between the sample surface and the incident beam was approximately 45°. Fluorescence-detected X-ray absorption spectra at the manganese K-edge were collected using a 13-element Ge detector (Ultra-LEGe detector, Canberra GmbH) installed perpendicular to the incident X-ray beam. Elemental analyses were carried out using a PerkinElmer 240 elemental analyzer. Atomic absorption analyses were done by using Varian Spectra AA-220 equipment.

X-ray crystallography

The diffraction data for **1** were collected at 80(2) K on a κ-geometry four-circle diffractometer (Xcalibur R diffractometer with a Ruby CCD detector equipped with an Oxford Cryosystems open-flow nitrogen cryostat), using graphite-monochromated Mo Kα radiation (λ = 0.71073 Å). Data were corrected for Lorentz, polarization and absorption effects. Data collection, cell refinement and data reduction and analysis were carried out with CryAlis PRO. The structure was solved with SHELXS-2018[45] and refined with the full-matrix least-squares procedure on F^2 using SHELXL-2018,[46] with anisotropic thermal parameters for all non-hydrogen atoms. Hydrogen atoms were found in the difference Fourier maps or were included using geometrical considerations. In the final refinement cycles, all H atoms were repositioned in their calculated positions and refined using a riding model. The structure plots were prepared using Diamond.[47] Crystallographic data for the crystal are listed in Table 2.

Crystallographic data (excluding structural factors) for structural analysis have been deposited with the Cambridge Crystallographic Data Centre, no. 1920522 for **1**.†

Table 2 Crystallographic data for **1**

CCDC no.	1920522
Formula	$C_{94}H_{172.60}Ca_4Mn_6O_{48.30}{\cdot}C_2H_3N$
Formula weight	2606.72
Crystal system	Orthorhombic
Space group	*Pbca*
a (Å)	22.242(5)
b (Å)	15.656(4)
c (Å)	38.588(8)
V (Å^3)	13 437(5)
Z	4
D_x (g cm^{-3})	1.289
F(000)	5500
μ(mm^{-1})	0.78
Crystal shape, color	Block, dark red
Crystal size (mm)	0.32 × 0.24 × 0.17
Θ range (°)	2.8–30.1
hkl range	−31 → 28, −21 → 21, −49 → 53
Measured reflections	42 436
Independent reflections	17 896
Reflections with $I > 2\sigma(I)$	11 421
R_{int}	0.048
R [$F^2 > 2\sigma(F^2)$]	0.072
w$R(F^2)$	0.171
Goodness of fit	1.07
Parameters	750
$\Delta\rho_{min}/\Delta\rho_{max}$ (e Å^{-3})	−0.80/1.33

Conflicts of interest

There are no conflicts to declare.

Acknowledgements

MMN and YM are grateful to the Institute for Advanced Studies in Basic Sciences and the National Elite Foundation for financial support. RB thanks the Imam Khomeini International University and the National Elite Foundation for financial support. We thank the Bundesministerium fuer Bildung und Forschung (BMBF; Operando-XAS project) and the Deutsche Forschungsgemeinschaft (DFG; cluster of excellence on Unifying Systems Catalysis, UniSysCat) for financial support. We acknowledge the Helmholtz-Zentrum Berlin (HZB) for providing access to the KMC-3 beamline of the BESSY synchrotron in Berlin-Adlershof; experimental support provided by Ivo Zizak and also the staff of the BESSY synchrotron is gratefully acknowledged. We thank Michael Haumann, Katharina Klingan, Chiara Pasquini, and Paul Kubella for their contributions to data collection and analysis. This research was also supported by the Ningbo Municipal Natural Science Foundation (Grant No. 2018A610183).

References

1 J. W. Ager and A. A. Lapkin, *Science*, 2018, **360**, 707–708.
2 N. S. Lewis and D. G. Nocera, *Proc. Natl. Acad. Sci. U. S. A.*, 2006, **103**, 15729–15735.
3 J. Liu, Y. Liu, N. Liu, Y. Han, X. Zhang, H. Huang, Y. Lifshitz, S.-T. Lee, J. Zhong and Z. Kang, *Science*, 2015, **347**, 970–974.
4 J. Luo, J.-H. Im, M. T. Mayer, M. Schreier, M. K. Nazeeruddin, N.-G. Park, S. D. Tilley, H. J. Fan and M. Grätzel, *Science*, 2014, **345**, 1593–1596.
5 R. D. Smith, M. S. Prévot, R. D. Fagan, Z. Zhang, P. A. Sedach, M. K. J. Siu, S. Trudel and C. P. Berlinguette, *Science*, 2013, 1233638.
6 Q. Yin, J. M. Tan, C. Besson, Y. V. Geletii, D. G. Musaev, A. E. Kuznetsov, Z. Luo, K. I. Hardcastle and C. L. Hill, *Science*, 2010, 1185372.

7 K. N. Ferreira, T. M. Iverson, K. Maghlaoui, J. Barber and S. Iwata, *Science*, 2004, **303**, 1831–1838.
8 M. Suga, F. Akita, K. Hirata, G. Ueno, H. Murakami, Y. Nakajima, T. Shimizu, K. Yamashita, M. Yamamoto and H. Ago, *Nature*, 2015, **517**, 99.
9 M. Suga, F. Akita, K. Hirata, G. Ueno, H. Murakami, Y. Nakajima, T. Shimizu, K. Yamashita, M. Yamamoto, H. Ago and J.-R. Shen, *Nature*, 2015, **517**, 99.
10 K. Yamaguchi, S. Yamanaka, H. Isobe, M. Shoji, K. Miyagawa, T. Nakajima, T. Kawakami and M. Okumura, *Physiol. Plant.*, 2019, **166**, 44–59.
11 I. D. Young, M. Ibrahim, R. Chatterjee, S. Gul, F. D. Fuller, S. Koroidov, A. S. Brewster, R. Tran, R. Alonso-Mori and T. Kroll, *Nature*, 2016, **540**, 453.
12 G. C. Dismukes, R. Brimblecombe, G. A. Felton, R. S. Pryadun, J. E. Sheats, L. Spiccia and G. F. Swiegers, *Acc. Chem. Res.*, 2009, **42**, 1935–1943.
13 T. Ghosh and G. Maayan, *Angew. Chem.*, 2019, **131**, 2811–2816.
14 J. S. Kanady, E. Y. Tsui, M. W. Day and T. Agapie, *Science*, 2011, **333**, 733–736.
15 H. B. Lee and T. Agapie, *Inorg. Chem.*, 2019, **58**(22), 14998–15003.
16 A. Mishra, W. Wernsdorfer, K. A. Abboud and G. Christou, *Chem. Commun.*, 2005, 54–56.
17 S. Mukherjee, J. A. Stull, J. Yano, T. C. Stamatatos, K. Pringouri, T. A. Stich, K. A. Abboud, R. D. Britt, V. K. Yachandra and G. Christou, *Proc. Natl. Acad. Sci. U. S. A.*, 2012, **109**, 2257–2262.
18 C. Zhang, C. Chen, H. Dong, J.-R. Shen, H. Dau and J. Zhao, *Science*, 2015, **348**, 690–693.
19 M. D. Karkas, O. Verho, E. V. Johnston and B. r. Åkermark, *Chem. Rev.*, 2014, **114**, 11863–12001.
20 J. P. McEvoy and G. W. Brudvig, *Chem. Rev.*, 2006, **106**, 4455–4483.
21 M. M. Najafpour, G. Renger, M. Hołyńska, A. N. Moghaddam, E.-M. Aro, R. Carpentier, H. Nishihara, J. J. Eaton-Rye, J.-R. Shen and S. I. Allakhverdiev, *Chem. Rev.*, 2016, **116**, 2886–2936.
22 W. Rüttinger and G. C. Dismukes, *Chem. Rev.*, 1997, **97**, 1–24.
23 M. Yagi and M. Kaneko, *Chem. Rev.*, 2001, **101**, 21–36.
24 K. J. Young, B. J. Brennan, R. Tagore and G. W. Brudvig, *Acc. Chem. Res.*, 2015, **48**, 567–574.
25 F. M. Ashmawy, C. A. McAuliffe, R. D. Parish and J. Tames, *J. Chem. Soc., Chem. Commun.*, 1984, 14–16.
26 M.-N. Collomb, A. Deronzier and J. Pe, *New J. Chem.*, 1999, **23**, 351–354.
27 S. Cooper and M. Calvin, *Science*, 1974, **185**, 376–376.
28 Z. Han, K. T. Horak, H. B. Lee and T. Agapie, *J. Am. Chem. Soc.*, 2017, **139**, 9108–9111.
29 E. A. Karlsson, B. L. Lee, T. Åkermark, E. V. Johnston, M. D. Kärkäs, J. Sun, Ö. Hansson, J. E. Bäckvall and B. Åkermark, *Angew. Chem., Int. Ed.*, 2011, **50**, 11919–11922.
30 W. T. Lee, S. B. Muñoz III, D. A. Dickie and J. M. Smith, *Angew. Chem.*, 2014, **126**, 10014–10017.
31 J. Limburg, J. S. Vrettos, L. M. Liable-Sands, A. L. Rheingold, R. H. Crabtree and G. W. Brudvig, *Science*, 1999, **283**, 1524–1527.
32 Y. Naruta, M. a. Sasayama and T. Sasaki, *Angew. Chem., Int. Ed. Engl.*, 1994, **33**, 1839–1841.
33 M. Watkinson, A. Whiting and C. A. McAuliffe, *J. Chem. Soc., Chem. Commun.*, 1994, 2141–2142.
34 Y. Yan, J. S. Lee and D. A. Ruddy, *Inorg. Chem.*, 2015, **54**, 4550–4555.
35 G. Maayan, N. Gluz and G. Christou, *Nat. Catal.*, 2018, **1**, 48.
36 R. K. Hocking, R. Brimblecombe, L.-Y. Chang, A. Singh, M. H. Cheah, C. Glover, W. H. Casey and L. Spiccia, *Nat. Chem.*, 2011, **3**, 461.
37 M. Najafpour, A. N. Moghaddam, H. Dau and I. Zaharieva, *J. Am. Chem. Soc.*, 2014, **136**, 7245–7248.
38 A. Singh, R. K. Hocking, S. L.-Y. Chang, B. M. George, M. Fehr, K. Lips, A. Schnegg and L. Spiccia, *Chem. Mater.*, 2013, **25**, 1098–1108.
39 Y.-Y. Li, K. Ye, P. E. M. Siegbahn and R.-Z. Liao, *ChemSusChem*, 2017, **10**, 903–911.
40 M. J. Frisch, G. W. Trucks, H. B. Schlegel, G. E. Scuseria, M. A. Robb, J. R. Cheeseman, G. Scalmani, V. Barone, G. A. Petersson, H. Nakatsuji, X. Li, M. Caricato, A. V. Marenich, J. Bloino, B. G. Janesko, R. Gomperts, B. Mennucci, H. P. Hratchian, J. V. Ortiz, A. F. Izmaylov, J. L. Sonnenberg, D. Williams-Young, F. Ding, F. Lipparini, F. Egidi, J. Goings, B. Peng, A. Petrone, T. Henderson, D. Ranasinghe, V. G. Zakrzewski, J. Gao, N. Rega, G. Zheng, W. Liang, M. Hada, M. Ehara, K. Toyota, R. Fukuda, J. Hasegawa, M. Ishida, T. Nakajima, Y. Honda, O. Kitao, H. Nakai, T. Vreven, K. Throssell, J. A. Montgomery Jr., J. E. Peralta, F. Ogliaro, M. J. Bearpark, J. J. Heyd, E. N. Brothers, K. N. Kudin, V. N. Staroverov, T. A. Keith, R. Kobayashi, J. Normand, K. Raghavachari, A. P. Rendell, J. C. Burant, S. S. Iyengar, J. Tomasi, M. Cossi, J. M. Millam, M. Klene, C. Adamo, R. Cammi, J. W. Ochterski, R. L. Martin, K. Morokuma, O. Farkas, J. B. Foresman and D. J. Fox, *Gaussian 16 Rev. C.01*, Wallingford, CT, 2016.
41 M. M. Najafpour, N. J. Moghaddam, S. M. Hosseini, S. Madadkhani, M. Hołyńska, S. Mehrabani, R. Bagheri and Z. Song, *Catal.: Sci. Technol.*, 2017, **7**, 3499–3510.
42 E. S. Ilton, J. E. Post, P. J. Heaney, F. T. Ling and S. N. Kerisit, *Appl. Surf. Sci.*, 2016, **366**, 475–485.
43 M. M. Najafpour, *Dalton Trans.*, 2011, **40**, 9076–9084.
44 M. M. Najafpour, M. Fekete, D. J. Sedigh, E.-M. Aro, R. Carpentier, J. J. Eaton-Rye, H. Nishihara, J.-R. Shen, S. I. Allakhverdiev and L. Spiccia, *ACS Catal.*, 2015, **5**, 1499–1512.
45 Rigaku, *CrysAlis PRO software. 1.171.38.43, v., Ed*, 2015.
46 G. M. Sheldrick, *Acta Crystallogr., Sect. C: Struct. Chem.*, 2015, **71**, 3–8.
47 K. Brandenburg, *Diamond (Version 3.2), Crystal and Molecular Structure Visualization, Crystal Impact–K*, ed. H. Putz and K. Brandenburg GbR, Bonn, Germany, 2009.